Trajectory Design and Navigation Analysis of a PLAsma TOrch Rocket Propelled Space Tug.

Edoardo Ciccarelli[1], Nicola Baresi[1], Nicolò Bernardini[2], Emin Saridede[1], Mansur Tisaev[1], Zhou Daniel Hao[3], Andrea Lucca Fabris[1], and Craig Underwood[1]

[1]Surrey Space Centre, University of Surrey,Guildford, UK
[2]Surrey Satellite Technology Ltd, Guildford, UK
[3]University of Leicester, Leicester, UK

Abstract—**PLATOR is a new electrothermal thruster for space logistics applications, developed by the University of Surrey and the University of Leicester. This paper describes the technology behind the development of the thruster and presents a mission scenario where a PLATOR-propelled spacecraft is used to capture and de-orbit the European Space Agency (ESA)'s Envisat satellite. The orbital transfer trajectory is designed using a time-optimal control approach, and the spacecraft's state vector's uncertainties are assessed through a covariance analysis. A navigation analysis is then performed to evaluate the spacecraft's capability to autonomously track its motion during the transfer using GPS measurements. Finally, a target proximity phase is then simulated to demonstrate the spacecraft's capability to rendezvous and dock with Envisat, using the uncertainties obtained from the covariance analysis, showing the potential of the PLATOR thruster for in-orbit servicing and active debris removal applications.**

I. INTRODUCTION

The PLAsma TOrch Rocket (PLATOR) project, funded by the UK Space Agency's Enabling Technologies Programme, aims to develop a new electrothermal thruster for space logistics applications. The project, carried out by a partnership between the University of Surrey and the University of Leicester, includes the experimental development of the thruster and the evaluation of its application to target in-orbit servicing and space transportation missions. In the PLATOR thruster, the propellant is partially ionised and heated up via radiofrequency electromagnetic fields and subsequently accelerated through a nozzle. This approach allows the propellant to reach extremely high temperatures and be efficiently accelerated, obtaining a hybrid performance point that fills the gap between high-thrust chemical propulsion solutions and high specific impulse electric propulsion engines.

This paper describes an assessment of the flight performance capabilities of this new thruster by presenting a reachability analysis of the orbits that can be achieved starting from low-Earth polar orbits achievable from UK launch facilities under development. Using an optimized Q-law, we demonstrate that a PLATOR-propelled spacecraft can reach commercially interesting orbits, including Sun-synchronous orbits and trans-lunar trajectories. Covariance and navigation analyses are later performed to assess the uncertainties with which the spacecraft's motion can be tracked during these transfers. These analyses are performed by processing ground stations' radiometric observables, collected every minute whenever the spacecraft is in view, and range measurements from GPS satellites. The 3σ covariance envelopes, stochastic ΔV budgets, and dispersion analyses obtained via our simulations will be fundamental to properly characterize the propellant requirements of different mission scenarios and drive the development of a PLATOR-propelled space tug for in-orbit servicing and active debris removal applications. The latter capabilities are demonstrated via a rendezvous and docking scenario that takes our uncertainties as an input for the proximity phase between the PLATOR-propelled space tug and an ENVISAT-like satellite at the end of its nominal mission.

II. PLATOR THRUSTER

Electrothermal thrusters (ET) form a subset of electric propulsion systems that leverage electric power to generate a high-temperature flow that is subsequently expanded and accelerated through a nozzle. Typically, ETs employ electrodes or electrical heating elements to increase the temperature of the propellant flow, although these components often impose limitations due to material constraints [1]. For instance, resistojets utilise heating elements that are restricted by material thermal limits, thereby setting a constraint on the achievable temperatures, and rely on the efficiency of the heat exchange process. In arcjets, the transfer of electric power to the propellant gas is accomplished via a plasma arc between electrodes, which are subject to notable erosion and vaporization [1]–[3]. In contrast, microwave electrothermal thrusters (METs) and inductively coupled plasma (ICPs) thrusters are compelling alternatives owing to their capability to achieve high temperatures (exceeding 10,000 K [4], [5]) with an electrodeless configuration [6]–[13]. METs leverage microwaves within a resonant cavity to generate plasma for propellant heating. ICPs utilise radio frequency (RF) antennas for generating a thermal plasma, through which the propellant flow can reach the aforementioned high-temperature range. RF currents create the inductive time-varying fields inside the thruster chamber and couple power to electrons, sustaining the plasma and heating up the propellant flow via electron-neutral collisions. The electrodeless nature of such devices fosters reduced erosion and therefore potential extended lifetimes. ICPs find diverse industrial applications including material processing, spectrometry, and high-power aerodynamic tests [6], [7]. Despite extensive industrial use, the application of

ICPs as thrusters remains relatively unexplored. Early proposals for ICP-based electrothermal thrusters emerged in the 1960s [14], with significant experimentation occurring in the 1980s and 1990s [12], [15], [16]. Subsequent studies explored power ranges from 50 W to 5 kW, revealing the versatility of ICPs with a wide range of propellants, including reactive ones [17]–[24]. Notably, investigations emphasised the significance of operating pressures, with 100 Torr identified as a crucial threshold for optimal performance, as the heating of the propellant depends on the collisional frequency [25], [26]. Recent experimental examinations of ICPs have yielded promising results. Oya et al. [27] operated a 100 W water propellant RF thruster at 3 MHz, achieving a specific impulse of 340 s and 3.6 mN thrust. Lafleur et al. [6] developed a theoretical model for an argon plasma ICP thruster, predicting thrust values of 100 mN and specific impulses of 500 s at power levels ranging from 300 to 500 W. Fujino and Yamauchi et al. [26] constructed a 2D RF ICP model, highlighting the impact of thermal losses, particularly at low pressures. Additionally, Pascale et al. [7] investigated the effects of gas injection methods on RF ICPs, demonstrating a 50% increase in thermal efficiency with reverse vortex injection of argon propellant at power levels up to 1 kW.

The PLATOR thruster is an electrothermal ICP-based system sized to operate at approximately 2000 W from the spacecraft bus, generating 200 mN of thrust with a specific impulse of 500 s. These reference figures are estimated utilising a thermodynamic model of the thruster. Stagnation conditions include a pressure of approximately 1 atm, a temperature of 4000 K, and a propellant water mass flow rate of 50 mg/s.

III. PLATOR SPACECRAFT PLATFORM DESIGN

The PLATOR spacecraft is designed to be a generic servicing platform for the on-orbit replenishment and repair of spacecraft, as well as for the capture and de-orbiting of satellites that pose a threat to the sustainability of the Low-Earth Orbit (LEO) environment.

The baseline design envisages an all-up wet mass of 1 tonne, of which 35% is to be allocated to the PLAsma TOrch Rocket (PLATOR) propellant, i.e., pure water. The mass envelope has been selected based on the PLATOR's high power requirements and variety of launch vehicles capable of delivering a 1 tonne spacecraft to LEO such as the Lockheed Martin/ABL Space Systems' RS1 Rocket, supposedly launching from the UK SaxaVord Spaceport in 2024/2025[1]. Complying with the ABL's Payload User Guidelines[2], the PLATOR spacecraft body is based on a regular nonagonal 9-sided prism with a diameter and height of approximately 2 m each. Internally, the PLATOR spacecraft will have a tri-axial symmetry with three large spherical propellant tanks filled with $\simeq$ 135 l of water and separated by three avionics stacks and their associated equipment. Such a design is an enlarged version of UoSAT-12, which was launched in 1999 following very similar design principles [28].

The baseplate -X facet will house the PLATOR main engine, launch vehicle attach fitting, and 4 blocks of resistojet thrusters for the Reaction Control System (RCS) and reaction wheels' de-saturation manoeuvres. Four more blocks of resistojets are envisaged on the +X facet of the spacecraft for the same purposes, along with a Universal Docking Adaptor like the Lockheed Martin's Mission Augmentation Port (MAP[3]). PLATOR will also carry the Rapidly Attachable Fluid Transfer Interface (RAFTI) fuelling port, which is being adopted by several in-orbit servicing companies such as Orbit Fab[4].

Up to 9 deployable solar panels will be mounted off the -X facet, forming a 9-fingered star arrangement. Combined with 9 body-mounted and 7-payload-bay-mounted panels, the 64×187.5 cm arrays will be able to guarantee a working solar array voltage of 45 V operating at a current of 4.8 A per panel under AM0 illumination (32% efficiency with solar flux of 1367 W m^{-2}). The remaining two sides of the payload bay are left for a pair of robot arms that will handle the capture and servicing of satellites. A render of the baseline PLATOR platform is shown in Fig. 1. Four 30 cm diameter brass reaction wheels of 4 cm depth will provide the necessary agility of the spacecraft in de-spinning large spacecraft platforms such as ESA's Envisat.
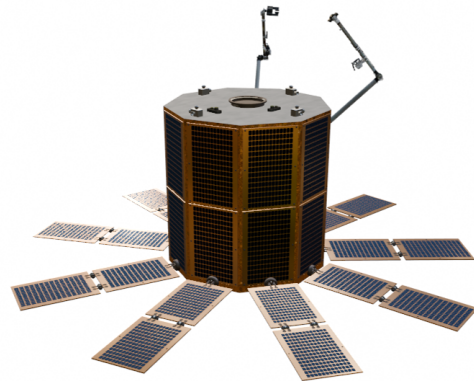
Fig. 1: Baseline PLATOR platform.

IV. TRANSFER TRAJECTORY DESIGN

The working mission scenario of this article is the capture of the ESA's 8-tonne Envisat satellite, which is currently out of control in a 770 km altitude Sun-Synchronous Orbit (SSO) with eccentricity $e = 0.00042$. It is assumed that the PLATOR spacecraft will be released in a 500-km altitude orbit and in the same orbital plane of Envisat with $i = 98.4°$. Such an orbital plane can be reached from the UK SaxaVord spaceport currently under development in the UK[5]($0°\,47'\,32.8''$ longitude; $60°\,49'\,5''$ latitude; available launch azimuths between 330 and 75 degrees from true north[6]). Both the right ascension of the ascending node and argument of periapsis are assumed to be zero.

To calculate a transfer trajectory from the initial Earth parking orbit to the orbit of Envisat, the initial and target orbit elements of the spacecraft are first converted into equinoctial ones following the notation of Olikara [29]. Gauss Variational Equations are implemented along with numerical averaging and control parametrization to allow time-optimal trajectories to be found with a relatively small number of control variables, namely the states of the PLATOR spacecraft (equinoctial elements plus mass), the transfer time, t_f, and the costate vector $\boldsymbol{\lambda}$ at user-defined control nodes. The nodes are found by re-scaling the independent variable of the problem to allow for the dynamics of the spacecraft to be integrated between $[-1, 1]$ [30]. Next, the re-scaled time domain is split into $K + 2$ sub-intervals $[\tau_i, \tau_{i+1}]$, $i = 1, \ldots, K + 1$ according to the roots of a $K = 64$ Legendre polynomials with $\tau = (2\,t - (t_0 + t_f))/(t_f - t_0)$. In the following, it is assumed that $t_0 = 0$ s. Both the states and the costates are finally approximated using Lagrange interpolating polynomials $\mathcal{L}_i(\tau)$ such that:

$$\boldsymbol{X}(\tau) = \sum_{i=1}^{K+1} \boldsymbol{X}(\tau_i)\,\mathcal{L}_i(\tau), \tag{1a}$$

$$\boldsymbol{\lambda}(\tau) = \sum_{i=1}^{K+1} \boldsymbol{\lambda}(\tau_i)\,\mathcal{L}_i(\tau), \tag{1b}$$

where

$$\mathcal{L}_i(\tau) = \prod_{j=1, j \neq i}^{K+1} \frac{\tau - \tau_j}{\tau_i - \tau_j}. \tag{2}$$

Equation (1a) can be differentiated to yield a numerical approximation for the τ derivative of $\boldsymbol{X}$ such that

$$\dot{\boldsymbol{X}}_i \simeq \sum_{i=1}^{K+1} D_{ki}\,\boldsymbol{X}(\tau_k) = \frac{(t_f - t_0)}{2}\boldsymbol{f}(\boldsymbol{X}_i, \boldsymbol{\lambda}_i), \tag{3}$$

where $\boldsymbol{X}_j = \boldsymbol{X}(\tau_j)$, $\boldsymbol{\lambda}_j = \boldsymbol{\lambda}(\tau_j)$, $\forall \tau_j \in [-1, +1]$, $\boldsymbol{f}(\boldsymbol{X}(\tau_i), \boldsymbol{\lambda}(\tau_i))$ is the averaged dynamics of the controlled two-body problem and D_{ki} is the differentiation matrix (see Ref. 30 for details). No Earth eclipses are simulated in the following, resulting in a transfer trajectory whereby the PLATOR engine is always on. The performance point of the thruster is as described in Section II with $I_{sp} = 450$ s, $T_{max} = 0.2$ N, and direction is driven by the costates of the problem:

$$\hat{\boldsymbol{u}}(\boldsymbol{X}, L, \boldsymbol{\lambda}) := \frac{M(\boldsymbol{X}, L)^T\,\boldsymbol{\lambda}}{\|M(\boldsymbol{X}, L)^T\,\boldsymbol{\lambda}\|}, \tag{4}$$

where L is the true longitude of the spacecraft, and M is the mapping matrix obtained from the Gauss Variational Equations of the equinoctial elements (see Ref. 29 for details).

Using Eq. (1), (3), and

$$\boldsymbol{X}_f = \boldsymbol{X}_0 + \frac{t_f - t_0}{2} \sum_{k=1}^{K} \omega_k\,\boldsymbol{f}(\boldsymbol{X}_k, \boldsymbol{\lambda}_k, t_f), \tag{5}$$

with ω_k as the quadrature weights of the K−th order Legendre polynomial [30], the optimal control problem can be transcribed into the Non-Linear Programming (NLP) problem of minimising t_f subject to:

$$\sum_{i=1}^{K+1} D_{ki}\,\boldsymbol{X}_k - \frac{(t_f) - t_0}{2}\boldsymbol{f}(\boldsymbol{X}_i, \boldsymbol{\lambda}_i; t_f) = \boldsymbol{0}, \tag{6a}$$

$$\boldsymbol{X}_f - \boldsymbol{X}_0 - \frac{t_f - t_0}{2} \sum_{k=1}^{K} \omega_k\,\boldsymbol{f}(\boldsymbol{X}_k, \boldsymbol{\lambda}_k; t_f) = \boldsymbol{0}, \tag{6b}$$

$$\|\boldsymbol{\lambda}_i\| - 1 = 0, \tag{6c}$$

for $i = 1, \ldots, K+1$. Note that Eq. (6c) has been added to aid with the convergence of the NLP problem, as recommended in Ref. 29. Figure 2 discloses the time-optimal trajectory obtained upon the convergence of the algorithm via the shareware software SNOPT [31]. According to this reference trajectory, PLATOR takes approximately 8.18 days and 32 kg of water propellant to insert into Envisat's orbit.
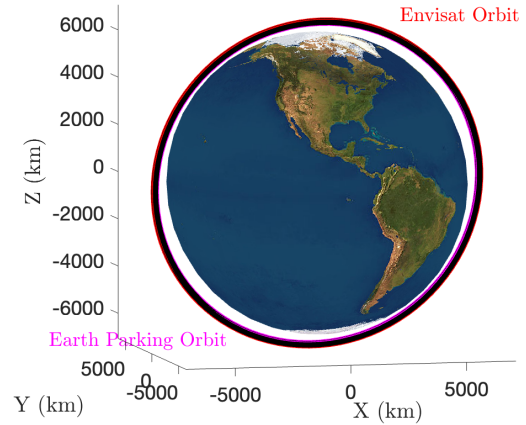
Fig. 2: PLATOR time-optimal transfer trajectory.

V. Knowledge Analysis

A. Analyisis setup

A covariance analysis was performed to assess the uncertainties with which the spacecraft's motion can be tracked during the transfer. The focus was on the spacecraft's state vector, which includes the position and velocity components, and the biases affecting the observables.

The analysis was performed by processing ground stations' radiometric observables and pseudorange measurements from GPS satellites. The models used for the observables are described in the following paragraphs.

1) Radiometric data: Three ground stations are assumed to be available for the mission, Gonhilly in the UK, one in Australia, and another in Argentina, to provide a wide coverage of the spacecraft's motion during the transfers. They provide range and range rate measurements, which can be then processed to obtain the state vector of the spacecraft. One-way range data between the spacecraft and the ground stations can be recovered from the elapsed time between the transmission of a signal from the ground station and the reception of the same signal by the spacecraft. Similarly, range

rate data can be obtained by measuring the Doppler shift of the signal's frequency, which is proportional to the relative velocity between the spacecraft and the ground station. For this analysis we assumed idealized models for radiometric data, not considering clock errors and tropospheric and ionospheric delays, only assuming a white noise and a bias affecting the measurements. The models used for the radiometric data are therefore:

$$\rho = \sqrt{(\boldsymbol{r} - \boldsymbol{r}_{St_i})^T (\boldsymbol{r} - \boldsymbol{r}_{St_i})} + \epsilon_\rho$$
$$\dot{\rho} = \frac{(\boldsymbol{r} - \boldsymbol{r}_{St_i})^T}{\rho} (\dot{\boldsymbol{r}} - \dot{\boldsymbol{r}}_{St_i}) + \epsilon_{\dot{\rho}} \quad (7)$$

where $\boldsymbol{r}$ and $\dot{\boldsymbol{r}}$ are the spacecraft's position and velocity vectors in the J2000 inertial reference frame, similarly $\boldsymbol{r}_{St_i}$ and $\dot{\boldsymbol{r}}_{St_i}$ are the ith ground station's position and velocity vectors, and ϵ_ρ and $\epsilon_{\dot{\rho}}$ are the biases affecting the measurements.

Data are collected every minute, whenever the minimum elevation angle for the spacecraft is at least $20°$ above the ground station's local horizon. These data are corrupted with white noise, with standard deviations as reported in Table I, and the position of the ground stations is assumed to be known with a 1 cm uncertainty.

2) GPS data: Similarly, to model GPS's data, a pseudo-range model was used, assuming a white noise and a bias affecting the measurements. The constellation of GPS satellites has been extracted from the GPS almanack, and the position of the satellites is assumed to be deterministically known.

The signal transmitted by the GPS's satellites is received by the spacecraft if the angle between the GPS's satellite nadir pointing line of sight vector and PLATOR is smaller than $20°$. A list of the collected pseudo ranges is therefore obtained by measuring the time of flight of the different signals, and the pseudo-range model is:

$$\rho_{GPS} = \sqrt{(\boldsymbol{r} - \boldsymbol{r}_{GPS})^T (\boldsymbol{r} - \boldsymbol{r}_{GPS})} + \epsilon_{\rho_{GPS}} \quad (8)$$

The pseudo ranges are collected every 3 minutes, and the data are corrupted with white noise, with a standard deviation as reported in Table I.

TABLE I: Frequency and standard deviation of the white noise added to the observations [32].

Measurement	Frequency	Noise standard deviation
Range	$1\ min$	σ_ρ=2 m
Range rate	$1\ min$	$\sigma_{\dot{\rho}}$=3 × 10^{-4} m/s
GPS range	$3\ min$	σ_{GPS}=10 m

B. Analyisis Results

The described observables are generated along the nominal trajectory of the spacecraft and they are processed through a Consider Extended Kalman filter to verify the observability of the system and quantify the uncertainties' evolution over time during the transfer. The filter is initialized with the a priori uncertainties reported in Table II, and the biases affecting the observables are estimated as part of the state vector.

The cartesian 'x', 'y', and 'z' components of the position and velocity vectors have been rotated in the radial 'ρ', along-track 'v', and cross-track 'k' components with respect to the

TABLE II: A priori uncertainties for the problem state vector components.

Object	Estimated quantities	σ a priori uncertainty
Plator	Position components	300 m
	Velocity components	0.3 m/s
Bias	Range	1 km
	Range rate	1×10^{-3} km/s
	GPS	1 km
	Consider parameters	
Ground Stations	Position	1 cm

local vertical local horizontal frame of the spacecraft following the spacecraft's motion. This was done by recalling the definition of covariance for a vector $\boldsymbol{X} = [x, y, z, v_x, v_y, v_z]$ of random variables, as:

$$\boldsymbol{P} = cov(\boldsymbol{X}, \boldsymbol{X})$$
$$= E[(\boldsymbol{X} - E[\boldsymbol{X}])(\boldsymbol{X} - E[\boldsymbol{X}])^T] \quad (9)$$
$$= E[\boldsymbol{X}\boldsymbol{X}^T] - E[\boldsymbol{X}]E[\boldsymbol{X}^T]$$

Therefore, given the desired rotation matrix $\boldsymbol{R}$ and the fact that the rotation $\boldsymbol{X}' = \boldsymbol{R}\boldsymbol{X}$ is a linear transformation, the covariance matrix of the rotated state vector can be obtained as:

$$\boldsymbol{P}' = \boldsymbol{R}\boldsymbol{P}\boldsymbol{R}^T \quad (10)$$

As Figure 3 shows, the state vector can be accurately estimated, with the position and velocity 3σ covariance envelopes decreasing immediately as the filter starts processing the synthetically generated data. The 3σ envelopes of the position vector decrease rather quickly and start to oscillate around $20 - 35$ meters depending on the amount of GPS satellites in view and with deeps in correspondence of the ground stations' passes. Similarly, the velocity vector's uncertainties decrease and oscillate in the range between 0.45 and 0.55 m/s, with similar behaviour to the position vector's uncertainties when radiometric data becomes available.

The biases affecting the observables are estimated as part of the state vector, and their estimated value over time, together with their 3σ covariance envelopes, are shown in Figure 4. Also in this case, the biases are estimated with good accuracy, and their uncertainties decrease over time, converging to a few meters for the range, a few mm/s for the range rate bias, and a few tens of meters for the GPS bias.

VI. Navigation Analysis

Building on the results of the covariance/knowledge analysis of Section V, a navigation analysis of the PLATOR mission scenario was executed to estimate the dispersions of the spacecraft's orbit elements upon insertion into the Envisat' orbit.

Relying on GPS measurements, the time-optimal trajectory of the spacecraft was recalculated anytime the distance between the PLATOR's estimated orbit and the nominal trajectory of Section IV was greater than 10 km. Additionally, the time-optimal trajectory of the spacecraft was recalculated any time the residual time-of-flight of PLATOR was less than 1 day, so as to reduce navigation errors ahead of insertion into Envisat's orbit.
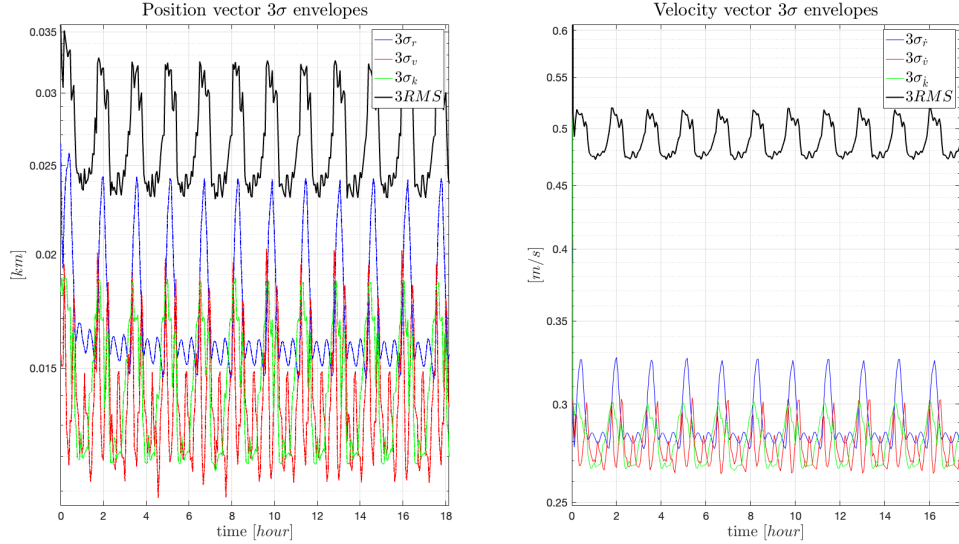
Fig. 3: PLATOR state's vector uncertainties over time in the first day of the transfer.
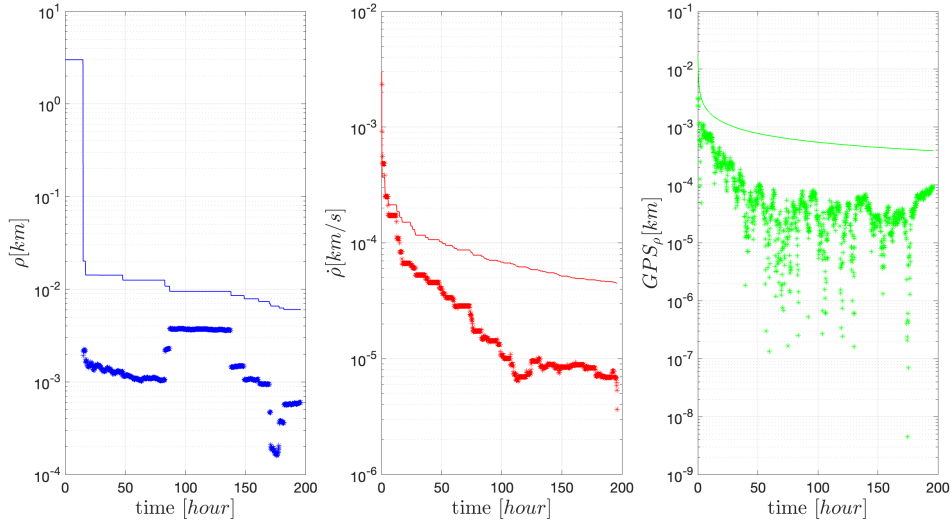
Fig. 4: 3σ covariance envelopes for the biases affecting the observables and their estimated value over time.

The timeline of the preliminary PLATOR rendezvous mission scenario is disclosed in Fig. 5 and was analyzed with a Monte Carlo simulation of 100 samples drawn from the spacecraft's a-priori covariance matrix of $P_0 = \text{diag}[\sigma_{Pos}^2, \sigma_{Pos}^2, \sigma_{Pos}^2, \sigma_{Vel}^2, \sigma_{Vel}^2, \sigma_{Vel}^2]$, where $\sigma_{Pos} = 10$ m and $\sigma_{Vel} = 10$ cm/s, respectively. The latter assume that the onboard Kalman filter of PLATOR has converged to the threshold values of Section V before the PLATOR engine is switched on to initiate the transfer. Figure 6 illustrates the results of the Monte Carlo simulation in terms of total time-of-flight, spacecraft's final mass, and differences with respect to the target semi-major axis, eccentricity, inclination, and right ascension of the ascending node (RAAN).

It should be noted that the trajectory optimization procedure of Section IV does not allow for targeting of the actual Envisat location along its orbit. However, a simple rephasing manoeuvre could be implemented at the end of the nominal transfer so as to rendezvous with the Envisat satellite ahead of proximity operations. In the following, it will be assumed that the PLATOR spacecraft has completed such a re-phasing manoeuvre and successfully reached the location of Envisat with a 10 km offset in the negative along-track direction.

VII. PROXIMITY PHASE

This section of the paper presents: 1) a preliminary conceptual design of the Guidance, Navigation, and Control (GNC) system for the PLATOR deorbit chaser spacecraft; 2) an analysis of the estimated the ΔV required for the rendezvous and proximity operations (RPO) to achieve final approach and clamping onto Envisat (c.f., Fig. 7).

The PLATOR chaser aims to safely approach Envisat, rigidly clamp onto it using robotic arms, and then deorbit it using the PLATOR engine. Table III lists the components of the GNC system. Water will be used for both the resistojets and the PLATOR thrusters, with the former being selected for the proximity operations instead of the main spacecraft
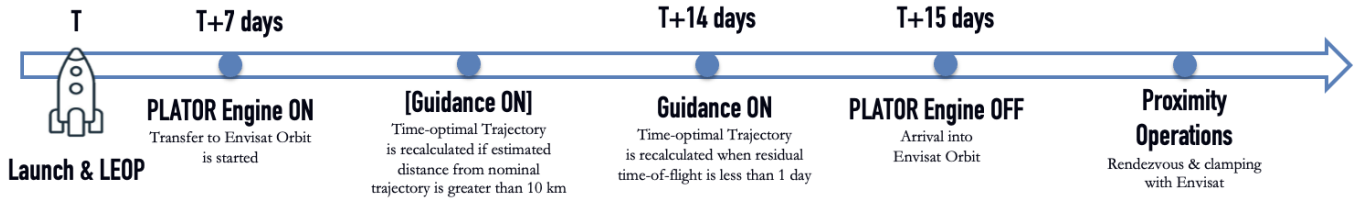
Fig. 5: PLATOR rendezvous mission scenario timeline.
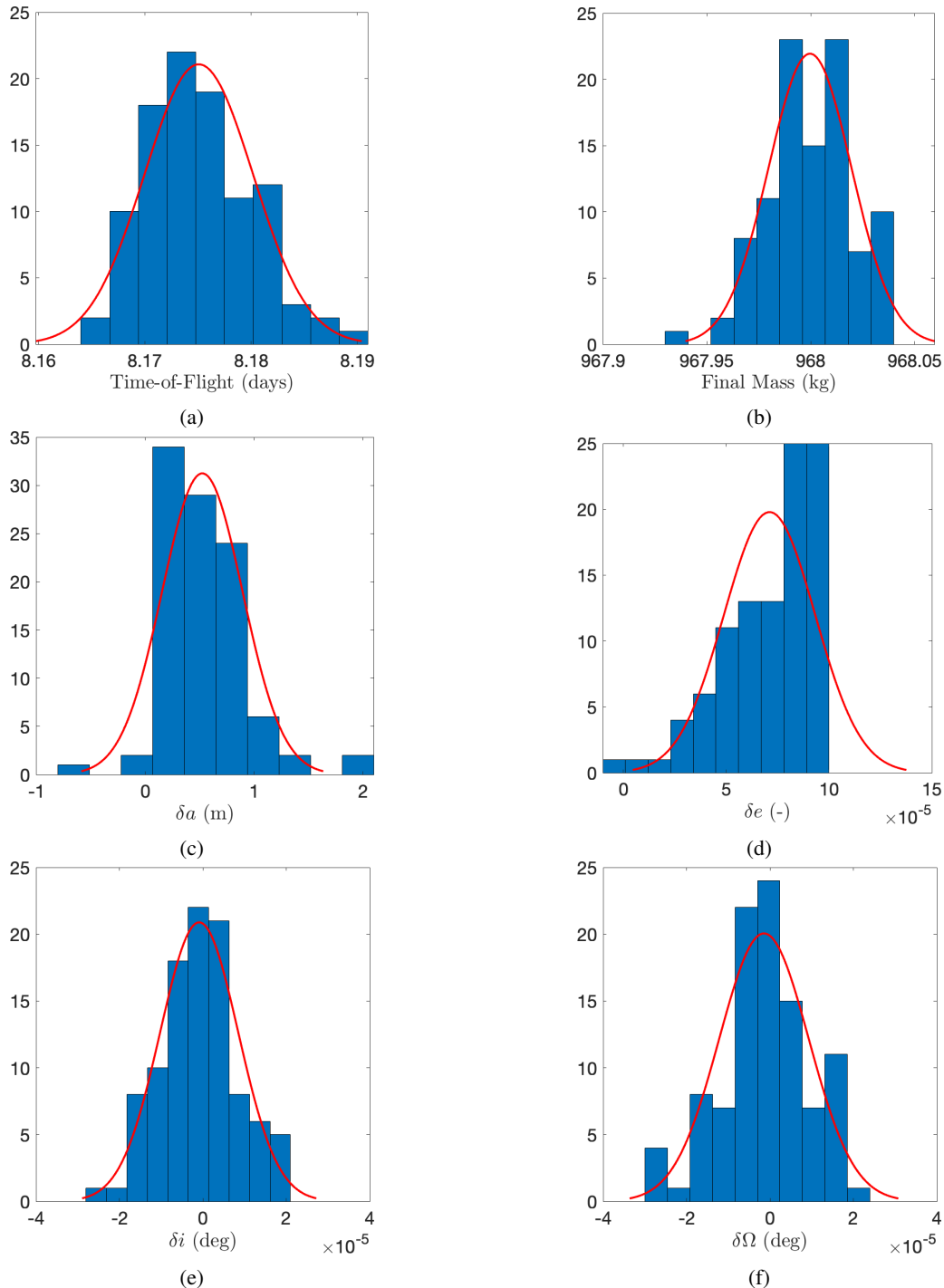
Fig. 6: Final Plator dispersions with respect to the nominal orbit elements of the Envisat spacecraft
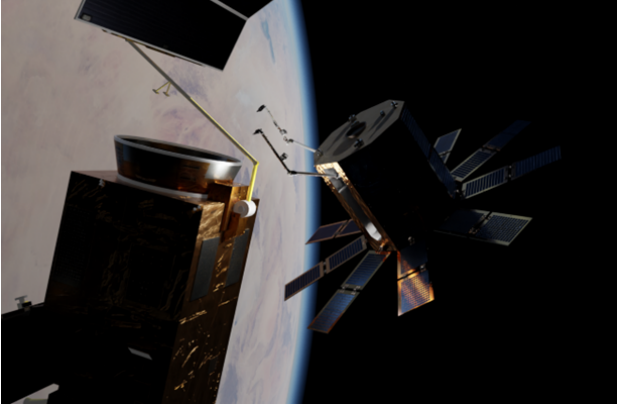
Fig. 7: The PLATOR deorbit spacecraft is in the final approach phase and ready to clamp onto the release ring of Envisat.

engine owing to the lack of details on the PLATOR's pulse characteristics and actual sizing at the moment of writing. Attitude control will be managed by the reaction wheels assembly and resistojets, even though attitude simulations are not currently included in our mission scenario.

TABLE III: GNC Hardware for PLATOR Close-proximity Operation

GNC Hardware	Uses
Resistojets	Attitude control and fine and higher forces close-range rendezvous manoeuvres
Camera (Wide lens for close-range, Telescope lens for mid- and far- range, eye-in-hand camera for clamping)	Computer vision based visual navigation (target pose estimation, close-range target survey)
LiDAR and Radar	Target characterisation, close range distance measuring
IMU and GPS	Positioning and attitude determination

Rendezvous and Close Proximity Operation trajectories Design and ΔV approximation

The primary focus of this section is to estimate the ΔV required for a given scenario of close-range rendezvous. This estimation will serve as a baseline reference for analysing fuel capacity in the context of the PLATOR deorbit spacecraft design. Accordingly, we do not consider real-time closed-loop simulations with uncertainties in the relative navigation, attitude, and control actions of the satellite.

For the simplified analyses of this section, Envisat is assumed to be in a perfectly circular sun-synchronous orbit with semi-major axis, inclination, and right ascension of the ascending node as specified in Section IV. The orientation of the target spacecraft is assumed to be parallel to its local-vertical local-horizontal (LVLH) reference frame (i.e., principal axes aligned with the radial, along-track, and cross-track direction), spinning about its maximum axis of inertia and completing one revolution per orbital period. This is a fairly gross assumption as Envisat is known to be spinning in an uncontrolled fashion with the longer arm controlling the orientation of the tail solar panel shifted towards the lower (-z) part of the spacecraft [33], [34].

Taking into account the orientation of the tail solar panel and the location of the release ring of the spacecraft (which is assumed to be the strongest structure of Envisat), we propose to approach the target from its positive along-track direction. The proposed approach includes performing a fly-around maneuver to survey the current conditions of Envisat in situ as suggested in Fig. 8, [35]. The starting position for the close-range rendezvous is assumed to be 10 km along the retrograde V-bar direction, i.e., the negative along-track direction of the Envisat's LVLH frame. S1 is the final entry gate before PLATOR starts maneuvering towards the S2 point located at +1 km in the along track direction. From there, the spacecraft reduces its relative distance with respect to the target by applying (mostly) tangential maneuvers that lower its along-track offset by 900 m and maneuver the chaser in the S3 point located at +100 m in the positive along-track direction. Here, PLATOR commences a fly-around manoeuvre that takes it to the S3a point where $\delta x = +50$ m in the radial direction with $\delta \dot{y} = -2\,n_{env}\,\delta_x$ and $n_{env} = 0.00104$ rad/s as negative along-track velocity and Envisat's mean motion, respectively. These relative conditions are known to insert the chaser spacecraft into a passive relative orbit about the target with nominal relative orbit period of $P_{env} \simeq 6010$ s [36], [37]. Indeed, the spacecraft is left to coast towards the S3b point, opposite to S3a, before the resistojet engines are switched on again to further reduce the altitude of the satellite till the S4 gate, located +20 m away in the Envisat's anti-Earth direction. At S4, the spacecraft hovers for 5 minutes, ideally collecting important measurements of its relative state with respect to the target before the final approach and grasping maneuvers are executed in S5. S5 is located at -5 m in the negative along-track direction.

The relative dynamics of the chaser as seen with respect to the LVLH frame of the target is approximated via the Hill-Clohessy-Wiltshire equations (HCW, [38]) and controlled via energy-optimal maneuvers that are obtained from the minimization of the hamiltonian [39]

$$\mathcal{H} = \frac{1}{2}\,\boldsymbol{u}^T\,\boldsymbol{u} + \boldsymbol{p}^T\,(A\,\boldsymbol{X} + B\,\boldsymbol{u}), \tag{11}$$

where $\boldsymbol{X} = [\delta x, \delta y, \delta z, \delta \dot{x}, \delta \dot{y}, \delta \dot{z}]^T$ is the relative state of PLATOR, $\boldsymbol{u}$ are the control inputs, $\boldsymbol{p}$ are the costates, and

$$A = \begin{pmatrix} 0 & 0 & 0 & 1 & 0 & 0 \\ 0 & 0 & 0 & 0 & 1 & 0 \\ 0 & 0 & 0 & 0 & 0 & 1 \\ 3\,n_{env}^2 & 0 & 0 & 0 & 2\,n_{env} & 0 \\ 0 & 0 & 0 & -2\,n_{env} & 0 & 0 \\ 0 & 0 & -n_{env}^2 & 0 & 0 & 0 \end{pmatrix},$$

$$B = \begin{pmatrix} 0 & 0 & 0 \\ 0 & 0 & 0 \\ 0 & 0 & 0 \\ 1 & 0 & 0 \\ 0 & 1 & 0 \\ 0 & 0 & 1 \end{pmatrix}, \tag{12}$$

are the dynamics and input matrices of the HCW equations, respectively. It follows that

$$\boldsymbol{u}^* = -B^T\,\boldsymbol{p}, \tag{13}$$
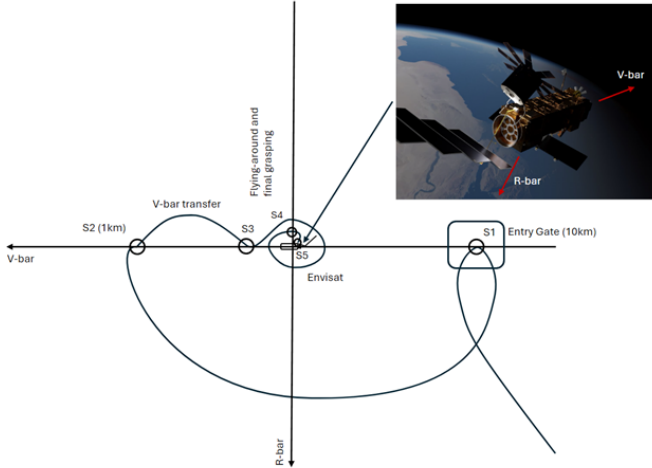
Fig. 8: An example of a Proximity Operations (PRO) scenario for the PLATOR deorbit chaser to clamp onto Envisat includes: 1) S1 to S2 involves V-bar tangential thrust manoeuvres to move from -10 km to +1 km relative to the target; 2) S2 to S3 includes another set of tangential thrust manoeuvres to close the distance to being 100 m away from Envisat along the +V-bar; 3) S3 to S4 will involve a fly-around executed by tangential impulse; 4) S4 is for position keeping (5 minutes) before the final clamping; 5) S4 to S5 is the final approach motion.

Fig. 9: Close-range maneuvers from S3 to S4.

where $\boldsymbol{p}$ can be found from the analytical solution of the adjoint equation $\dot{\boldsymbol{p}} = -A^T \boldsymbol{p}$, as reported in Ref. [40]. Let $\Phi_p(t, t_0)$ denote the adjoint transition matrix such that

$$\boldsymbol{p}(t) = \Phi_p(t, t_0) \boldsymbol{p}_0, \tag{14}$$

$$\boldsymbol{X}(t) = \Phi_X(t, t_0) \boldsymbol{X}_0 + \int_{t_0}^{t} \Phi_X(t, \tau) \left(B\, B^T \right) \Phi_p(\tau, t_0) \boldsymbol{p}_0 \, \mathrm{d}\tau, \tag{15}$$

where $\boldsymbol{X}_0$ and $\boldsymbol{p}_0$ denote the initial state and initial costates, respectively, Φ_X is the state transition matrix associated with the general solution of the HCW equations [36], [40], and t_0 and t denote the initial and current time, respectively.

To find the initial costates that can drive the chaser towards a desired relative state with respect to the target, namely $\boldsymbol{X}^*$, Eq. (15) can be inverted as soon as a user-defined time-of-flight is chosen for the maneuver. The time-of-flights reported in Table IV have been selected to maintain compliance with the maximum resistojet thrust of 4×0.025 N and resulted in the trajectory and control profiles of Fig. 9. A Monte

TABLE IV: Time-of-flight for the different phases of the simplified rendezvous & grasping scenario.

	Time-of-flight
from S1 to S2	$3\,P_{env}$
from S2 to S3	$1.5\,P_{env}$
from S3 to S3a	$P_{env}/2$
from S3a to S3b	$P_{env}/2$
from S3b to S4	$P_{env}/2$
Hovering in S4	5 minutes
S4 to S5	$P_{env}/2$

Carlo simulation of 1000 samples obtained by perturbing the nominal initial conditions in S1 with the probability density functions of Fig. 6 is finally implemented, resulting in the total ΔV cost and propellant mass of Fig. 10. It is found that the 99th percentile of the total ΔV cost is 1.1508 m/s, corresponding to 1.4184 kg of water propellant. This leaves plenty of resources for the de-orbiting of Envisat, even though more work is needed to quantify the costs of matching the attitude state of the target and ascertain the feasibility of de-spinning and de-orbiting the PLATOR plus Envisat pair.

VIII. CONCLUSION

The PLATOR thruster was presented in this article, briefly introducing the technology behind the development of the thruster and presenting a mission scenario where a PLATOR-propelled spacecraft is used to rendezvous with the ESA's Envisat satellite. The orbital transfer trajectory from an initial 500-km altitude sun-synchronous orbit to the current orbit of Envisat was designed using a time-optimal pseudo-spectral directo optimization approach, demonstrating the ability of the PLATOR platform to reach the target's 770-km altitude orbit in approximately 8.18 days with approximately 32 kg of water propellant. A covariance analysis was then performed to assess the uncertainties with which the spacecraft's motion can be tracked during the transfer, showing that the state vector can be accurately observed by processing radiometric data from ground stations and GPS satellites. As a result, a navigation analysis was initiated, whereby the optimal trajectory of the spacecraft was recomputed anytime the error between the reference and estimated trajectory of the satellite was greater than 10 km or if the remaining time-of-flight of the latter was less than 1 days. Numerical simulations showed that the orbit of envisat can be reached with relatively good accuracy despite the navigation errors affecting the initial conditions of the vehicle. Finally, the rendezvous of PLATOR with Envisat was simulated under the assumptions of the Hill-Clohessy-Wiltshire equations. Although more work is needed to add measurement models of proximity sensors such as LIDAR and cameras, numerical simulations have shown that PLATOR can successfully target the orbit of Envisat using a closed-loop energy-optimal control policy resulting in a total delta-V consumption of 1.15 m/s (99th percentile).
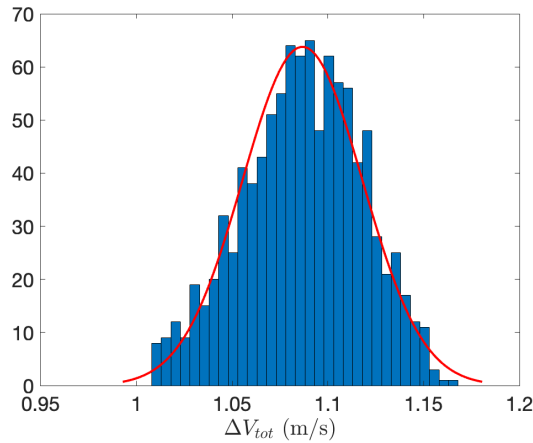
(a) Total ΔV consumption for simplified rendezvous & grasping scenario.
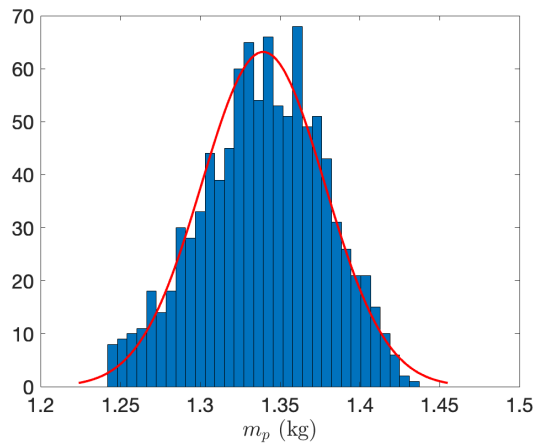
(b) Propellant mass for simplified rendezvous & grasping scenario.

Fig. 10: Results of 1000 sample Monte Carlo analysis for the energy-optimal simplified rendezvous & grasping scenario.

REFERENCES

[1] W. Harris, E. O'Hair, L. Hatfield, and M. Kristiansen, "Cathode erosion research on medium to high power arcjet thrusters," IEEE Transactions on Electron Devices, vol. 28, pp. 280–292, 1993.

[2] M. Nishida, K. Kaita, and K. Tanaka, "Numerical studies of the flow field in a dc arcjet thruster," in 20th International Electric Propulsion Conference, IEPC1988-105, Garmisch-Partenkirchen, West Germany, 3–6 October, 1988.

[3] M. Auweter-Kurtz, T. Gblz, H. Habiger, F. Hammer, H. Kurtz, M. Riehle, and C. Sleziona, "100 kw class hydrogen arcjet thruster," in 25th International Electric Propulsion Conference, IEPC-97-007, Cleveland, Ohio, USA, 24–28 August, 1997.

[4] M. Boulos, "Rf induction plasma spraying: State-of-the-art review," Journal of thermal spray technology, vol. 1, pp. 33–40, 1992.

[5] J. Mostaghimi and M. I. Boulos, "Effect of frequency on local thermodynamic equilibrium conditions in an inductively coupled argon plasma at atmospheric pressure," Journal of applied physics, vol. 68, no. 6, pp. 2643–2648, 1990.

[6] T. Lafleur and C. Corr, "Characterization of a radio-frequency inductively coupled electrothermal plasma thruster," Journal of Applied Physics, vol. 130, no. 4, 2021.

[7] A. Pascale, T. Lafleur, and C. Corr, "Bidirectional vortex stabilization of a supersonic inductively coupled plasma torch," Journal of Physics D: Applied Physics, vol. 56, no. 10, p. 105202, 2023.

[8] J. R. Hopkins, M. M. Micci, S. G. Bilén, and S. G. Chianese, "Direct thrust measurements of an 8-ghz microwave electrothermal thruster," IEEE Transactions on Plasma Science, vol. 46, no. 6, pp. 2009–2015, 2018.

[9] J. L. Power, "Microwave electrothermal propulsion for space," IEEE transactions on microwave theory and techniques, vol. 40, no. 6, pp. 1179–1191, 1992.

[10] S. G. Chianese and M. M. Micci, "Microwave electrothermal thruster chamber temperature measurements and performance calculations," Journal of propulsion and power, vol. 22, no. 1, pp. 31–37, 2006.

[11] M. Micci, S. Bilén, and D. Clemens, "History and current status of the microwave electrothermal thruster," Progress in Propulsion Physics, vol. 1, pp. 425–438, 2009.

[12] M. M. Micci, "Radio-frequency and microwave thrusters," Encyclopedia of Aerospace Engineering, 2010.

[13] M. S. Yildiz and M. Celik, "Plume diagnostics of bustlab microwave electrothermal thruster using langmuir and faraday probes," Plasma Science and Technology, vol. 21, no. 4, p. 045505, 2019.

[14] A. Mironer and F. Hushfar, "Radio frequency heating of a dense, moving plasma," in Electric Propulsion Conference, 1963, p. 45.

[15] J. Pollard, D. Lichtin, and R. Cohen, "Rf discharge electrothermal propulsion-results from a lab-scale thruster," in 23rd Joint Propulsion Conference, 1987, p. 2124.

[16] L. Brewer, G. Frind, and T. Karras, Preliminary results of a high power RF thruster test. AIAA, 1989.

[17] R. Bond, A. Martin, A. Bond, C. Banks, and R. Eaton, "An experimental investigation of the performance of a radio-frequency thruster," in 21st International Electric Propulsion Conference, 1990, p. 2544.

[18] T. Rutledge, M. Micci, and S. Bilén, "Design and initial tests of a low power radio-frequency electrothermal thruster," in 44th AIAA/ASME/SAE/ASEE Joint Propulsion Conference & Exhibit, 2008, p. 4537.

[19] J. R. Hopkins, M. M. Micci, and S. G. Bilén, "Design and testing of a low power radio-frequency electrothermal thruster," in 31st International Electric Propulsion Conference, IEPC-2009-203, MI, USA, 20–24 September, 2009.

[20] D. Tsifakis, C. Charles, and R. Boswell, "An inductively-coupled plasma electrothermal radiofrequency thruster," Frontiers in Physics, vol. 8, p. 34, 2020.

[21] R. Georg, A. Chadwick, B. Dally, and G. Herdrich, "Resolving transient discharge cycle behaviour in modulated inductive plasmas," Vacuum, vol. 182, p. 109636, 2020.

[22] ——, "Power efficiency estimation of an inductive plasma generator using propellant mixtures of oxygen, carbon-dioxide and argon," Acta Astronautica, vol. 179, pp. 536–545, 2021.

[23] A. Chadwick, B. Dally, G. Herdrich, and M. Kim, "High-power inductive electric propulsion operation with alternative propellants," The Aeronautical Journal, vol. 124, no. 1272, pp. 151–169, 2020.

[24] J. E. Brandenburg, J. Kline, and D. Sullivan, "The microwave electrothermal (met) thruster using water vapor propellant," IEEE transactions on plasma science, vol. 33, no. 2, pp. 776–782, 2005.

[25] K. D. Diamant, B. L. Zeigler, and R. B. Cohen, "Microwave electrothermal thruster performance," Journal of propulsion and power, vol. 23, no. 1, pp. 27–34, 2007.

[26] T. Fujino and M. Yamauchi, "Numerical study of plasma-fluid characteristics and thrust performance of a low-power argon inductively coupled plasma electrothermal thruster," Journal of Applied Physics, vol. 128, no. 17, 2020.

[27] M. Oya, N. Yamamoto, and H. Nakashima, "Energy balance in a radio frequency electro-thermal thruster with water propellant," in 31st International Electric Propulsion Conference, IEPC-2009-203, MI, USA, 20–24 September, 2009.

[28] M. Fouquet and M. Sweeting, "Uosat-12 minisatellite for high performance earth observation at low cost," Acta Astronautica, vol. 41, no. 3, pp. 173–182, 1997.

[29] Z. P. Olikara, "Framework for optimizing many-revolution low-thrust transfers," in Paper AAS 18-332 presented at the AAS/AIAA Astrodynamics Specialist Conference, 2018.

[30] G. T. Huntington, "Advancement and analysis of a gauss pseudospectral trascription for optimal control problems," Ph.D. dissertation, MIT, 2003.

[31] P. E. Gill, W. Murray, and M. A. Saunders, "Snopt: An sqp algorithm for large-scale constrained optimization," SIAM review, vol. 47, no. 1, pp. 99–131, 2005.

[32] J. Leonard, B. Jones, E. Villalba, and G. Born, "Absolute orbit determination and gravity field recovery for 433 eros using satellite-to-satellite tracking," in AIAA/AAS Astrodynamics Specialist Conference, 2012, p. 4877.

[33] D. Kucharski, G. Kirchner, F. Koidl, C. Fan, R. Carman, C. Moore, A. Dmytrotsa, M. Ploner, G. Bianco, M. Medvedskij et al., "Attitude and spin period of space debris envisat measured by satellite laser ranging," IEEE Transactions on Geoscience and Remote Sensing, vol. 52, no. 12, pp. 7651–7657, 2014.

[34] R. Biesbroek, T. Soares, J. Husing, and L. Innocenti, "The e.Deorbit CDF Study: A Design Study for the Safe Removal of a Large Space Debris," in 6th European Conference on Space Debris, ser. ESA Special Publication, L. Ouwehand, Ed., vol. 723, Aug. 2013, p. 79.

[35] W. Fehse, Automated Rendezvous and Docking of Spacecraft, ser. Cambridge Aerospace Series.   Cambridge University Press, 2003.

[36] H. Schaub and J. L. Junkins, Analytical mechanics of space systems. Aiaa, 2003.

[37] D. P. Scharf, F. Y. Hadaegh, and S. R. Ploen, "Precision formation delta-v requirements for distributed platforms in earth orbit," in Enabling Sensor and Platform Technologies for Spaceborne Remote Sensing, vol. 5659.   SPIE, 2005, pp. 312–323.

[38] W. Clohessy and R. Wiltshire, "Terminal guidance system for satellite rendezvous," Journal of the aerospace sciences, vol. 27, no. 9, pp. 653–658, 1960.

[39] J. M. Longuski, J. J. Guzmán, and J. E. Prussing, Optimal control with aerospace applications.   Springer, 2014, vol. 32.

[40] H.-C. Cho and S.-Y. Park, "Analytic solution for fuel-optimal reconfiguration in relative motion," Journal of Optimization Theory and Applications, vol. 141, no. 3, pp. 495–512, 2009.